



Mechanistic insights into the interactions of TAX1BP1 with RB1CC1 and mammalian ATG8 family proteins

Mingfang Zhang^a , Yingli Wang^a , Xinyu Gong^a , Yaru Wang^{a,b} , Yuchao Zhang^a , Yubin Tang^a, Xindi Zhou^a, Haobo Liu^a, Yichao Huang^a, Jing Zhang^{a,c}, and Lifeng Pan^{a,b,c,1}

Edited by James Hurley, University of California, Berkeley, CA; received September 11, 2023; accepted February 2, 2024

TAX1BP1, a multifunctional autophagy adaptor, plays critical roles in different autophagy processes. As an autophagy receptor, TAX1BP1 can interact with RB1CC1, NAP1, and mammalian ATG8 family proteins to drive selective autophagy for relevant substrates. However, the mechanistic bases underpinning the specific interactions of TAX1BP1 with RB1CC1 and mammalian ATG8 family proteins remain elusive. Here, we find that there are two distinct binding sites between TAX1BP1 and RB1CC1. In addition to the previously reported TAX1BP1 SKICH (skeletal muscle and kidney enriched inositol phosphatase (SKIP) carboxyl homology)/RB1CC1 coiled-coil interaction, the first coiled-coil domain of TAX1BP1 can directly bind to the extreme C-terminal coiled-coil and Claw region of RB1CC1. We determine the crystal structure of the TAX1BP1 SKICH/RB1CC1 coiled-coil complex and unravel the detailed binding mechanism of TAX1BP1 SKICH with RB1CC1. Moreover, we demonstrate that RB1CC1 and NAP1 are competitive in binding to the TAX1BP1 SKICH domain, but the presence of NAP1's FIP200-interacting region (FIR) motif can stabilize the ternary TAX1BP1/NAP1/RB1CC1 complex formation. Finally, we elucidate the molecular mechanism governing the selective interactions of TAX1BP1 with ATG8 family members by solving the structure of GABARAP in complex with the non-canonical LIR (LC3-interacting region) motif of TAX1BP1, which unveils a unique binding mode between LIR and ATG8 family protein. Collectively, our findings provide mechanistic insights into the interactions of TAX1BP1 with RB1CC1 and mammalian ATG8 family proteins and are valuable for further understanding the working mode and function of TAX1BP1 in autophagy.

TAX1BP1 | RB1CC1 | GABARAP | autophagy receptor | selective autophagy

Autophagy is a multistep and tightly regulated lysosome-dependent catabolic process in mammals and plays vital roles in numerous physiological processes including cellular homeostasis, organelle quality control, immune response, and aging (1, 2). Concomitantly, dysfunctions of autophagy caused by mutations in autophagy genes are linked with many human disorders, such as immune disorders, cancer, and neurodegenerative diseases (2–4). Unlike conventional nonselective bulk autophagy that indiscriminately sequesters and degrades cytosolic components, selective autophagy, which is driven by dedicated adaptor proteins named autophagy receptors, can selectively recognize and target relevant substrates for autophagic degradations (5–8). So far, dozens of autophagy receptors and related selective autophagy have been uncovered (6–10), such as SQSTM1/p62, NBR1, Optineurin, TAX1BP1 for the selective autophagy of bulk protein aggregates (aggrephagy) (11–14), NDP52, TAX1BP1, Optineurin for the selective autophagy of invading pathogens (xenophagy) (15–17), Nix, FUNDC1 for the selective autophagy of mitochondria (mitophagy) (18, 19), FAM134B, Sec62, CCPG1, RTN3, TEX264, ATL3 for the selective autophagy of endoplasmic reticulum (ER-phagy) (20–26), STBD1 for the selective autophagy of glycogen (glycophagy) (27), and NCOA4 for the selective autophagy of ferritin (ferritinophagy) (28). Based on the recent progress in the selective autophagy field, in order to efficiently drive selective autophagy for specific autophagic cargoes, a typical autophagy receptor at least should possess three essential characteristics: 1) It should harbor a cargo-associating domain that can specifically recognize or reside on the targeting autophagic cargoes, such as the ubiquitin-binding domains of SQSTM1/p62, NBR1, Optineurin, NDP52, and TAX1BP1 or the transmembrane domains of Nix, FUNDC1, CCPG1, and FAM134B; 2) it should have the ability to recruit relevant autophagy machinery to initiate the *in situ* phagophore formation around the targeting autophagic cargoes; and 3) it should contain a LC3-interacting region (LIR) for recognizing the key ATG8 family proteins, which include six members (LC3A, LC3B, LC3C, GABARAP, GABARAPL1, and GABARAPL2) in mammals, to facilitate the autophagosome formation for engulfing the targeting autophagic cargoes as well as the related downstream selective autophagy process. However, many of the detailed molecular

Significance

TAX1BP1-mediated selective autophagy is crucial for the clearances of invading pathogens, proteotoxic aggregates, damaged mitochondria, and lysosomes in mammals and relies on the specific interactions of TAX1BP1 with RB1CC1 and mammalian ATG8 family proteins, but with poorly understood mechanisms. In this study, we present the biochemical and structural characterizations of the interactions of TAX1BP1 with RB1CC1 and ATG8 family proteins. We uncover the unique dual-binding-site mode between TAX1BP1 and RB1CC1, and report the crystal structures of the TAX1BP1 SKICH (SKIP carboxyl homology)/RB1CC1 and TAX1BP1/GABARAP complexes, which provide mechanistic insights into the interactions of TAX1BP1 with RB1CC1 and ATG8 family proteins.

Author affiliations: ^aState Key Laboratory of Chemical Biology, Shanghai Institute of Organic Chemistry, University of Chinese Academy of Sciences, Chinese Academy of Sciences, Shanghai 200032, China; ^bSchool of Chemistry and Materials Science, Hangzhou Institute for Advanced Study, University of Chinese Academy of Sciences, Hangzhou 310024, China; and ^cCollege of Chemistry and Materials Science, Sichuan Normal University, Chengdu, Sichuan 610068, China

Author contributions: M.Z. and L.P. designed research; M.Z., Yaru Wang, Y.Z., Y.T., X.Z., H.L., Y.H., and J.Z. performed research; M.Z., Yingli Wang, X.G., and L.P. analyzed data; and M.Z. and L.P. wrote the paper.

The authors declare no competing interest.

This article is a PNAS Direct Submission.

Copyright © 2024 the Author(s). Published by PNAS. This article is distributed under [Creative Commons Attribution-NonCommercial-NoDerivatives License 4.0 \(CC BY-NC-ND\)](#).

¹To whom correspondence may be addressed. Email: panlf@sioe.ac.cn.

This article contains supporting information online at <https://www.pnas.org/lookup/suppl/doi:10.1073/pnas.2315550121/-DCSupplemental>.

Published March 4, 2024.

mechanism governing the specific recruitments of relevant upstream autophagy machinery and ATG8 family proteins by autophagy receptors during selective autophagy are still poorly understood.

As a multifunctional adaptor protein in mammals, TAX1BP1 was initially identified as a cellular binding protein of the human T-lymphotropic virus 1 Tax protein (29) and later was demonstrated to function as a ubiquitin-binding autophagy receptor to participate in xenophagy and the depolarization-dependent mitophagy processes (16, 30–32). Recently, TAX1BP1 was also found to serve as a key autophagy receptor to mediate aggrephagy and lysophagy (the selective autophagy of damaged lysosome) (14, 33, 34). From the domain organization, TAX1BP1 contains an N-terminal SKIP carboxyl homology (SKICH) domain, three coiled-coil domains that are responsible for the dimerization of TAX1BP1 (35), and two C-terminal zinc-finger (ZF) domains (Fig. 1A). Specifically, the SKICH domain of TAX1BP1 has the ability to directly interact with the TBK1-binding adaptor NAP1 or SINTBAD (15, 36), thereby establishing an indirect association with the TBK1 kinase

(Fig. 1A). TBK1 is a noncanonical I κ B family kinase that plays a crucial role in various selective autophagy processes mediated by SQSTM1/p62, Optineurin, NDP52, and TAX1BP1 (17, 37–41). In addition to interacting with NAP1 or SINTBAD, the SKICH domain of TAX1BP1 can also directly bind to RB1CC1 (Fig. 1A), a key subunit of the autophagy initiation Unc-51-like kinase (ULK) complex (42), to facilitate the recruitment of the ULK complex for the initiation of autophagosome formation in TAX1BP1-mediated selective autophagy (33, 43). Intriguingly, TAX1BP1 can also cooperate with RB1CC1 to exert crucial roles for the autophagic clearances of NCOA4 and NBR1 through the unconventional “ATG8-independent autophagy” processes (44, 45), in addition to its roles as an autophagy receptor. Previously, we had determined the TAX1BP1 SKICH/NAP1 complex structure and elucidated the molecular mechanism governing the specific interaction between TAX1BP1 and NAP1 (36). However, how TAX1BP1 associates with RB1CC1 and the detailed relationship between RB1CC1 and NAP1 in binding to TAX1BP1 remain largely unknown.

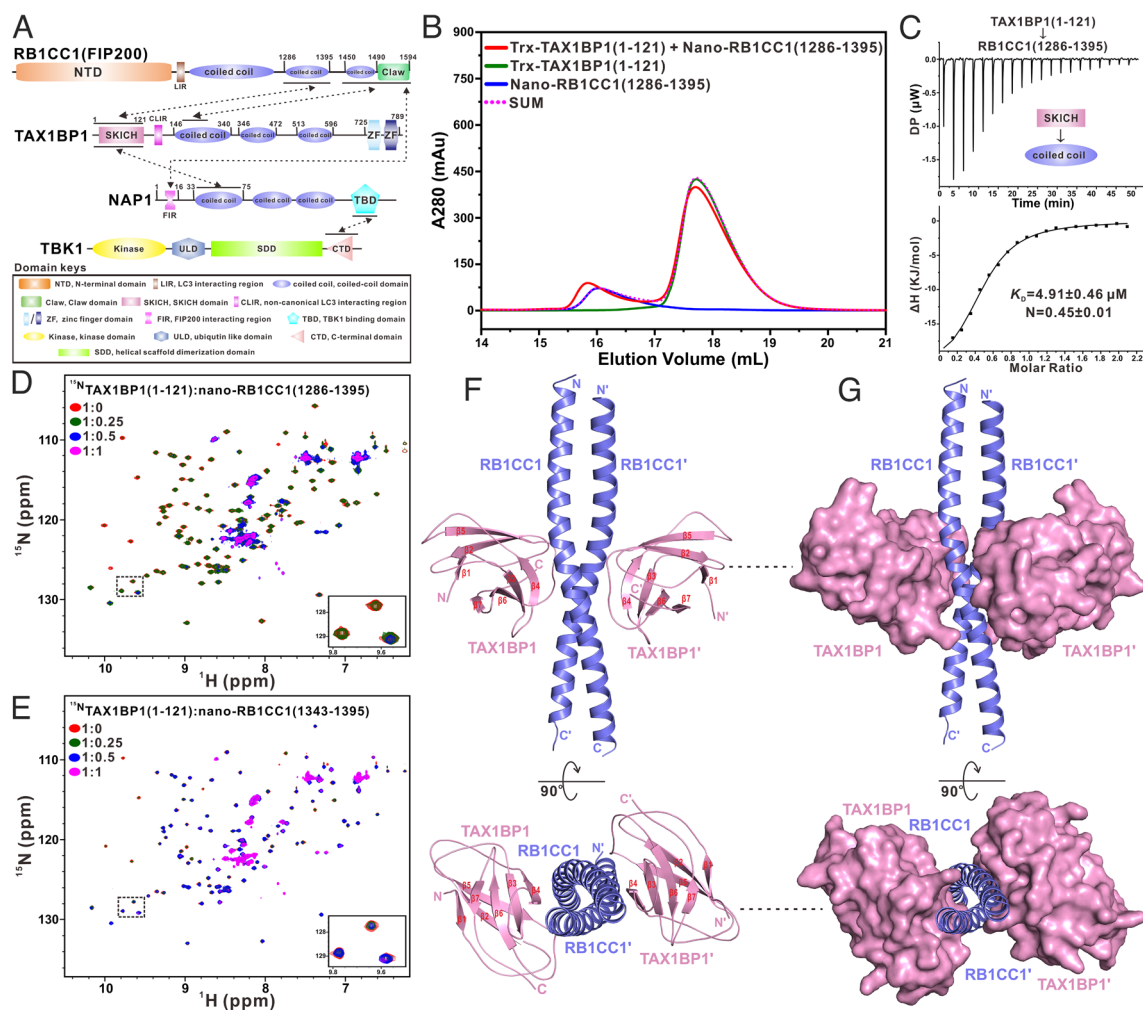


Fig. 1. Biochemical and structural characterizations of the interaction between the TAX1BP1 SKICH domain and RB1CC1 coiled-coil region. (A) A schematic diagram showing the domain organizations of RB1CC1, TAX1BP1, NAP1, and TBK1. In this drawing, the RB1CC1/TAX1BP1, RB1CC1/NAP1, TAX1BP1/NAP1, and NAP1/TBK1 interactions are further highlighted and indicated by two-way arrows. (B) Overlay plot of the SEC of RB1CC1(1286-1395) and TAX1BP1(1-121) as well as their mixture. A₂₈₀, the UV absorbance at 280 nm. (C) ITC-based measurement of the binding affinity of TAX1BP1(1-121) with RB1CC1(1286-1395). The dissociation constant (K_D) error is the fitted error obtained from the data analysis software when using the one-site binding model to fit the ITC data. DP, the differential power measured by the ITC machine. ΔH , the heat change measured by the ITC machine. (D and E) Superposition plots of the ^1H - ^{15}N HSQC spectra of ^{15}N -labeled TAX1BP1(1-121) titrated with the increasing molar ratios of RB1CC1(1286-1395) (D), or RB1CC1(1343-1395) (E). For clarity, each insert shows the enlarged view of a selected representative region in the overlaid ^1H - ^{15}N HSQC spectra. (F) Ribbon diagram showing the overall structure of TAX1BP1(1-121) in complex with RB1CC1(1343-1395). In this drawing, TAX1BP1(1-121) is shown in pink and RB1CC1(1343-1395) in slate. (G) Combined ribbon and surface representation showing the overall architecture of the TAX1BP1(1-121)/RB1CC1(1286-1395) complex with the same color scheme and orientation as in panel (F). The experiments depicted in this figure have been replicated once.

TAX1BP1 was reported to include two putative LIRs, a canonical LIR motif (CLIR) (residues 49 to 52, “WVGI”) within the N-terminal SKICH domain and a non-CLIR motif in the linker region connecting the SKICH and coiled-coil domains (30). However, based on the structure of the TAX1BP1 SKICH domain (36, 46), the putative CLIR motif of TAX1BP1 is unlikely to serve as a functional LIR motif, as it is buried in the structural core of the SKICH domain. The CLIR motif of TAX1BP1, which is similar to that of its parologue NDP52 (47), can differentially bind to six mammalian ATG8 orthologues (16). The C-terminal ZF region of TAX1BP1 is mainly responsible for the selective recognitions of relevant autophagic cargoes. In particular, the second ZF domain of TAX1BP1 can function as a ubiquitin-binding domain to recognize relevant ubiquitinated substrates for selective autophagic degradations (16, 48). Interestingly, the two ZF domains of TAX1BP1 were also proved to participate in the interaction of TAX1BP1 with the unconventional actin-based molecular motor Myosin VI (16, 48). Importantly, the simultaneous bindings of TAX1BP1 with Myosin VI and mammalian ATG8 orthologues decorated on the outer membrane of autophagosome can facilitate the fusion of autophagosome with endosome as well as the maturation of autophagosome (16, 31, 49). Accordingly, the specific interactions of TAX1BP1 CLIR with mammalian ATG8 family members are crucial for the multifaceted autophagic function of TAX1BP1. However, due to the lack of detailed structural investigations, the precise binding modes of TAX1BP1 CLIR with mammalian ATG8 family proteins remain elusive.

Here, we systematically characterize the interactions of TAX1BP1 with RB1CC1 and six mammalian ATG8 family proteins. We find that, in addition to the previously reported interaction between the TAX1BP1 SKICH/RB1CC1 coiled-coil, the first coiled-coil region of TAX1BP1 is capable of directly binding to the extreme C-terminal coiled-coil and Claw region of RB1CC1. The determined high-resolution crystal structure of the TAX1BP1 SKICH/RB1CC1 coiled-coil complex not only uncovers the detailed molecular mechanism governing the specific interaction between the SKICH domain of TAX1BP1 and RB1CC1 but also reveals that the SKICH domains of TAX1BP1 and NDP52 share a common binding mode to recognize RB1CC1. Furthermore, we demonstrate that the coiled-coil domains of NAP1 and RB1CC1 are mutually exclusive in binding to the SKICH domain of TAX1BP1. However, when NAP1’s FIR motif is present, a stable ternary complex comprising TAX1BP1, NAP1, and RB1CC1 can be formed, thereby facilitating the recruitment of TBK1. Additionally, we uncover that the CLIR motif of TAX1BP1 can selectively interact with six mammalian ATG8 orthologues and preferentially binds to GABARAP and GABARAPL1. We determine the structure of TAX1BP1 CLIR in complex with GABARAP and unveil the detailed molecular mechanism governing the specific interaction of TAX1BP1 with GABARAP. Finally, we demonstrate that TAX1BP1 alone, the TAX1BP1/RB1CC1 binary complex, and the TAX1BP1/NAP1/RB1CC1 ternary complex have different abilities for interacting with GABARAP.

Results

Biochemical Characterizations of the Interaction between RB1CC1 Coiled-Coil Region and the SKICH Domain of TAX1BP1. The SKICH domain of TAX1BP1 was previously implicated in the interaction of TAX1BP1 with the C-terminal coiled-coil region (residues 1286 to 1395) of RB1CC1 (33, 43, 44). Relevant sequence alignment analyses of the entire C-terminal region of RB1CC1, which encompasses the two C-terminal coiled-coil domains and the Claw domain (residues 1286 to 1594), and the full-length TAX1BP1 from different

eukaryotic species showed that the N-terminal SKICH domain (residues 1 to 121) of TAX1BP1 and the first C-terminal coiled-coil domain (residues 1286 to 1395) of RB1CC1 are highly conserved during evolution (*SI Appendix*, Figs. S1 and S2), in line with their established roles for facilitating the interaction between TAX1BP1 and RB1CC1 (33, 43, 44). Subsequently, the RB1CC1(1286–1395) and TAX1BP1(1–121) fragments were purified and subjected to a size exclusion chromatography (SEC)-based analysis to assess their potential direct interaction. Unexpectedly, based on our SEC result, there is an extremely weak peak shift on the SEC profile for the RB1CC1(1286–1395)/TAX1BP1(1–121) mixture sample (Fig. 1*B*), suggesting a direct interaction between RB1CC1(1286–1395) and TAX1BP1(1–121), albeit they are unable to form a stable binary complex. Consistently, subsequent analytical ultracentrifugation-based analyses showed that the measured sedimentation coefficient distribution of RB1CC1(1286–1395) in the mixture sample increases with the increasing amount of TAX1BP1(1–121) (*SI Appendix*, Fig. S3), confirming that TAX1BP1(1–121) can directly interact with RB1CC1(1286–1395) in solution. Importantly, our quantitative isothermal titration calorimetry (ITC) analysis demonstrated that TAX1BP1(1–121) can bind to RB1CC1(1286–1395) with a dissociation constant (K_D) value of ~4.91 μM (Fig. 1*C*). Regrettably, our attempts to further narrow down the TAX1BP1-binding region within the RB1CC1(1286–1395) fragment through ITC-based truncation analyses were failed (*SI Appendix*, Fig. S4). Given the distinctive capability of NMR spectroscopy in elucidating dynamic protein–protein interaction, we consequently employed NMR spectroscopy to examine the interaction between TAX1BP1(1–121) and RB1CC1 coiled-coil. As expected, the titration of the ¹⁵N-labeled TAX1BP1(1–121) with the unlabeled RB1CC1(1286–1395) proteins resulted in significant dose-dependent peak broadenings for the majority of peaks in the ¹H–¹⁵N HSQC spectrum of TAX1BP1(1–121) (Fig. 1*D*), confirming the direct interaction between TAX1BP1(1–121) and RB1CC1(1286–1395). Importantly, further NMR-based truncation analyses of RB1CC1(1286–1395) uncovered that the interaction between RB1CC1(1286–1395) and TAX1BP1(1–121) is primarily mediated by the C-terminal RB1CC1(1343–1395) segment rather than the N-terminal RB1CC1(1286–1342) segment (Fig. 1*E* and *SI Appendix*, Fig. S5). Notably, our sedimentation velocity analyses revealed that both RB1CC1(1343–1395) and RB1CC1(1286–1395) exist as a concentration-dependent monomer–dimer equilibrium state in solution (*SI Appendix*, Fig. S6). Specifically, RB1CC1(1343–1395) mainly exists as a monomer at low concentrations, but tends to form a dimer at higher concentrations (*SI Appendix*, Fig. S6*A* and *C*). We speculated that the different concentrations of RB1CC1(1343–1395) used for ITC and NMR experiments are the potential reasons why the RB1CC1(1343–1395) fragment displays obvious interaction with TAX1BP1 SKICH in our NMR experiments but not in our ITC assay (Fig. 1*E* and *SI Appendix*, Fig. S4*B*).

The Overall Structure of the TAX1BP1 SKICH/RB1CC1(1343–1395) Complex. Next, we decided to determine the TAX1BP1(1–121)/RB1CC1(1343–1395) complex structure to elucidate the molecular mechanism underlying the specific interaction between TAX1BP1(1–121) and RB1CC1(1343–1395). Since we failed to obtain a stable complex of TAX1BP1(1–121) with RB1CC1(1343–1395), the crystallization screening of the TAX1BP1(1–121)/RB1CC1(1343–1395) complex was carried out by directly using a protein mixture, which is prepared by mixing TAX1BP1(1–121) and RB1CC1(1343–1395) together in a 1:1 molar ratio. Based on this approach, we successfully obtained high-quality crystals that diffracted to a resolution of 2.39 Å (*SI Appendix*, Table S1). Utilizing molecular replacement method, we were able to determine the crystal

structure of the TAX1BP1(1-121)/RB1CC1(1343-1395) complex (*SI Appendix*, Table S1), which consists of two TAX1BP1 SKICH molecules and one parallel RB1CC1(1343-1395) coiled-coil dimer, forming a symmetrical 2:2 stoichiometric hetero-tetramer (Fig. 1 F and G). In the TAX1BP1(1-121)/RB1CC1(1343-1395) complex structure, the two TAX1BP1 SKICH molecules, each of which contains seven antiparallel β -strands forming a β -sandwich immunoglobulin-like architecture, symmetrically pack against the middle region of the RB1CC1(1343-1395) coiled-coil dimer (Fig. 1 F), each burying a total of $\sim 423 \text{ \AA}^2$ interface area (Fig. 1 G). Previously, the SKICH domain of TAX1BP1 had been proven to interact with NAP1 (15), and the structures of the isolated TAX1BP1 SKICH domain and the TAX1BP1 SKICH/NAP1 complex had already been determined (36, 46). Careful structural comparison analyses revealed that the overall configuration of the TAX1BP1 SKICH domain in the TAX1BP1(1-121)/RB1CC1(1343-1395) complex is very similar to that of the *apo*-form TAX1BP1 SKICH (PDB ID: 4NLH) and the TAX1BP1 SKICH domain in the TAX1BP1 SKICH/NAP1 complex (PDB ID: 5Z7G) (*SI Appendix*, Fig. S7 A and B). Intriguingly, further structure modeling analysis uncovered that the SKICH domain of TAX1BP1 employs two distinct binding sites, which locate on the opposite surfaces of TAX1BP1 SKICH, to associate with the dimeric coiled-coil domains of RB1CC1 and NAP1 (*SI Appendix*, Fig. S7C), revealing that the SKICH domain of TAX1BP1 can adopt different approaches to interact with RB1CC1 and NAP1.

The Molecular Interface of the TAX1BP1 SKICH/RB1CC1(1343-1395) Complex.

Further comprehensive structural analysis of the TAX1BP1 SKICH/RB1CC1(1343-1395) complex unveiled that the SKICH domain of TAX1BP1 relies on key interface residues from the β_3 and β_4 strands as well as the β_1/β_2 , β_3/β_4 , β_5/β_6 connecting loops to specifically interact with RB1CC1 residues located in the central region of the dimeric RB1CC1 coiled-coil through both hydrophobic and polar interactions (Fig. 2 A and B and *SI Appendix*, Fig. S8). Particularly, the backbone carboxyl groups of R61, Y63, Y64 together with the polar side chain groups of N29, Y63, Y64, W68, Q88, Y90, Y91, N94 from TAX1BP1 interact with the R1375, E1373, S1372, E1369, Q1361 residues

from one chain of the RB1CC1 dimer and the S1370, D1366, D1364, Q1360 residues from the other chain of the RB1CC1 dimer, forming 15 highly specific hydrogen bonds (Fig. 2 B). Furthermore, the side chains of K54, R61, and D62 residues from TAX1BP1 SKICH establish four pairs of salt bridges with the E1380, K1383 residues from one chain of the dimeric RB1CC1 coiled-coil as well as the E1381, D1374 residues from the other chain of the dimeric RB1CC1 coiled-coil (Fig. 2 B). In parallel, the hydrophobic side chain groups of Y63, T65, F66, Y90, and Y91 of TAX1BP1 SKICH pack against a hydrophobic patch formed by the hydrophobic side chains of L1367, L1371 residues from one RB1CC1 chain and the I1368 residue from the other chain of the dimeric RB1CC1 (Fig. 2 B). In line with their critical structural roles, these key binding interface residues of TAX1BP1 and RB1CC1 are highly conserved during evolution (*SI Appendix*, Figs. S1 and S2). Importantly, consistent with our structural data, further mutations of key residues involved in the binding interface of the TAX1BP1 SKICH/RB1CC1(1343-1395) complex, such as the R61A/D62A/Y63A and R61A/D62A/F66E triple mutations of TAX1BP1 SKICH or the L1367A, R1375A, E1381A mutations of RB1CC1(1286-1395), significantly decrease or completely disrupt the specific interaction between TAX1BP1 SKICH and RB1CC1(1286-1395) (Fig. 2 C-E and *SI Appendix*, Fig. S9).

Interestingly, in addition to TAX1BP1, NDP52 also possesses an N-terminal SKICH domain that can specifically bind to the C-terminal coiled-coil region of RB1CC1 (43, 50, 51). Previously, we had determined the crystal structure of the NDP52 SKICH/RB1CC1(1286-1395) complex (51). Relevant structural and sequence comparison analyses revealed that the overall binding mode of TAX1BP1 SKICH and RB1CC1(1343-1395) closely resembles that of the NDP52 SKICH/RB1CC1(1286-1395) interaction (*SI Appendix*, Fig. S10A), and unsurprisingly, the RB1CC1 coiled-coil employs many identical residues to interact with the SKICH domains of NDP52 and TAX1BP1 (*SI Appendix*, Fig. S1). Further sequence alignment analysis revealed that although there are variations in several residues involved in the interactions between RB1CC1 coiled-coil and the SKICH domains of NDP52 and TAX1BP1, these SKICH domains actually utilize many identical or highly similar interface residues to

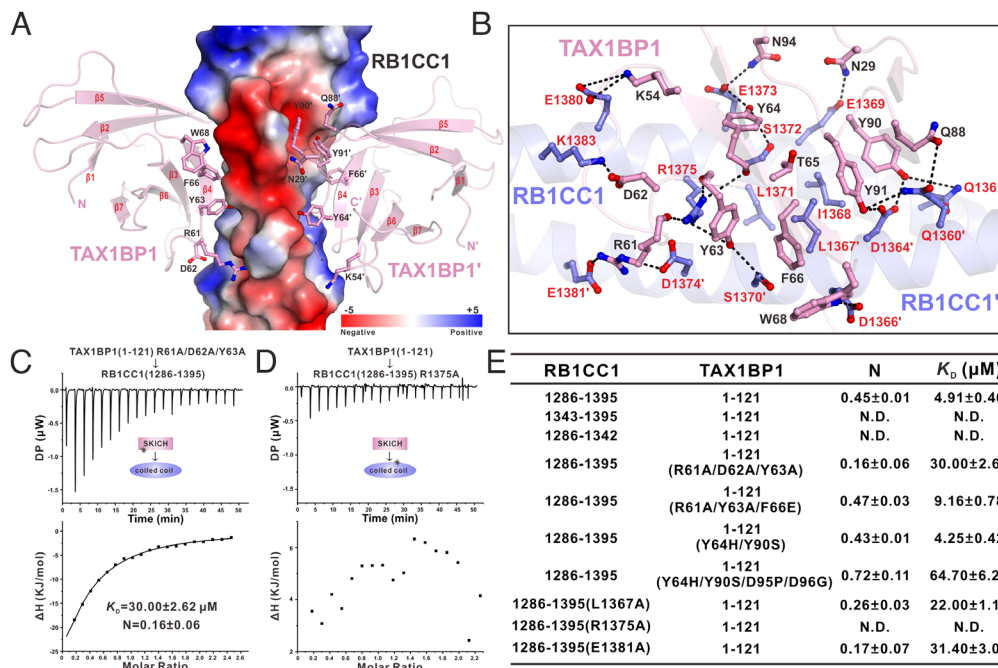


Fig. 2. The molecular interface of the TAX1BP1(1-121)/RB1CC1(1343-1395) complex. (A) The combined surface charge potential representation and the ribbon-stick model showing the detailed interactions between RB1CC1(1343-1395) and TAX1BP1(1-121) in the complex structure. (B) The ribbon-stick representation showing the binding interface between TAX1BP1 SKICH and RB1CC1 coiled-coil in the TAX1BP1(1-121)/RB1CC1(1343-1395) complex structure. The hydrogen bonds and salt bridges involved in the interaction are shown as dotted lines. (C and D) ITC-based measurements of the binding affinities of the TAX1BP1(1-121) R61A/Y62A/Y63A mutant with RB1CC1(1286-1395) (C), and TAX1BP1(1-121) with the RB1CC1(1286-1395) R1375A mutant (D). (E) The measured binding affinities between various forms of TAX1BP1(1-121) and RB1CC1(1286-1395) or their mutants by ITC-based assays. “N.D.” stands for that the K_D value is not detectable. The experiments depicted in this figure have been replicated once.

engage with the dimeric RB1CC1 coiled-coil (*SI Appendix*, Fig. S10B). Consistently, further SEC-based analyses confirmed that the SKICH domains of TAX1BP1 and NDP52 are unable to simultaneously bind to RB1CC1 coiled-coil (*SI Appendix*, Fig. S10C and D). Notably, the corresponding SKICH domain of CALCOCO1 lacks several crucial RB1CC1-binding interface residues, including Y64 and Y90 (*SI Appendix*, Fig. S10B). Based on systematic biochemical and structural analyses, we further demonstrated that the SKICH domain of CALCOCO1 cannot interact with RB1CC1 coiled-coil and rationalized why the SKICH domain of TAX1BP1 but not CALCOCO1 can bind to RB1CC1 (see *SI Appendix, Results* for a detailed description). In all, we concluded that the SKICH domains of TAX1BP1 and NDP52 share a general binding mode to interact with RB1CC1 coiled-coil, and are competitive in binding to RB1CC1, while the SKICH domain of CALCOCO1 can not interact with RB1CC1.

TAX1BP1 and RB1CC1 Contain Another Binding Site Except for the TAX1BP1 SKICH/RB1CC1 Coiled-Coil Site. Interestingly, unlike the monomeric TAX1BP1(1-121), the longer fragment TAX1BP1(1-237), which includes the SKICH domain, the CLIR motif and portions of the coiled-coil region of TAX1BP1 (*SI Appendix*, Fig. S2), forms a stable dimer in solution (*SI Appendix*, Fig. S12), and obviously interacts with RB1CC1(1286-1395) in our SEC-based assays (Fig. 3A). Further SEC-based analyses demonstrated that the R1375A mutation, which specifically disrupts the binding of TAX1BP1 SKICH with RB1CC1(1286-1395) (Fig. 2D), essentially abolishes the interaction between TAX1BP1(1-237) and RB1CC1(1286-1395) (Fig. 3B). In contrast, the R1375A mutant of RB1CC1(1286-1594) that encompasses the SKICH-binding coiled-coil domain together with the extreme C-terminal coiled-coil and Claw domain (Fig. 1A), still maintains a strong interaction with TAX1BP1(1-237) (Fig. 3C and D). Based on these observations, we inferred that there may exist additional binding sites between TAX1BP1 and RB1CC1, apart from the previously identified TAX1BP1 SKICH/RB1CC1 coiled-coil interaction. Consistent with our hypothesis, relevant co-immunoprecipitation assays demonstrated that the R1375A mutation that specifically disrupts the interaction between TAX1BP1 SKICH and RB1CC1 coiled-coil (Fig. 2D), only partially diminishes rather than completely abolishes the interaction between the full-length TAX1BP1 and RB1CC1 in cells (*SI Appendix*, Fig. S13). Importantly, further SEC and analytical ultracentrifugation-based analyses demonstrated that the RB1CC1(1396-1594) and RB1CC1(1450-1594) fragments, both of which contain the extreme C-terminal coiled-coil and Claw domains but lack the SKICH-binding coiled-coil domain of RB1CC1 (Fig. 1A), can directly interact with TAX1BP1(1-237) (*SI Appendix*, Figs. S14 A and C and S15 A and B), confirming the existence of an additional binding site between TAX1BP1 and RB1CC1. In contrast, the RB1CC1(1396-1449) fragment, which only comprises the linker region between the two C-terminal coiled-coil domains of RB1CC1, is unable to interact with TAX1BP1(1-237) (*SI Appendix*, Fig. S14B). Therefore, we concluded the RB1CC1(1450-1594) fragment contains an intact and un-reported binding site for TAX1BP1.

Subsequently, using spectral shift binding assays, we successfully determined the binding affinities of TAX1BP1(1-237) with RB1CC1(1286-1395), RB1CC1(1450-1594), and RB1CC1(1286-1594). Specifically, the binding affinity K_D value between TAX1BP1(1-237) and RB1CC1(1286-1395) measured by the spectral shift binding assay is about 1.13 μM (Fig. 3E), similar level to the K_D value obtained by the ITC approach (Fig. 1C). In contrast, the interaction between TAX1BP1(1-237) and RB1CC1(1450-1594) is very weak, and the measured K_D value is larger than 136 μM

(Fig. 3F). Interestingly, the measured K_D value of the interaction between TAX1BP1(1-237) and RB1CC1(1286-1594) is on the similar level as that of the interaction between TAX1BP1(1-237) and RB1CC1(1286-1395) (Fig. 3E and G). However, the spectral shift profiles observed in the TAX1BP1(1-237)/RB1CC1(1286-1395) interaction and the TAX1BP1(1-237)/RB1CC1(1286-1594) interaction have totally different patterns (Fig. 3E and G), suggesting that the binding mode of RB1CC1(1286-1594) with TAX1BP1(1-237) is distinct from that of the RB1CC1(1286-1395)/TAX1BP1(1-237) interaction. Notably, based on the three K_D values obtained by the spectral shift binding assays, the two binding sites of RB1CC1 do not exhibit a synergistic effect in binding to TAX1BP1. Subsequently, through systematic biochemical and structural analyses, we further revealed that the second binding site between RB1CC1 and TAX1BP1 is mainly mediated by the interaction between RB1CC1(1450-1594) and the coiled-coil region of TAX1BP1 (residues 146 to 237) (see *SI Appendix, Results* for a detailed description).

The NAP1 FIR/RB1CC1 Claw and NAP1 Coiled-Coil/TAX1BP1 SKICH Interactions Are Essential for the Formation of the Stable TAX1BP1/NAP1/RB1CC1 Ternary Complex. Our structural analyses showed that the SKICH domain of TAX1BP1 relies on two separated and nonoverlapping binding interfaces to recognize the coiled-coil domains of RB1CC1 and NAP1 (*SI Appendix*, Fig. S7C), implying the possibility of the simultaneous binding of RB1CC1 and NAP1 to the SKICH domain of TAX1BP1. To elucidate the precise relationship between the coiled-coil domains of RB1CC1 and NAP1 in binding to TAX1BP1 SKICH, we performed relevant SEC and analytical ultracentrifugation-based assays. Our SEC-based biochemical results unraveled that NAP1(33-75) and RB1CC1(1286-1395) are mutually exclusive in binding to TAX1BP1(1-237) (*SI Appendix*, Fig. S18 A-D). Consistently, NAP1(33-75) is unable to associate with the binary TAX1BP1(1-237)/RB1CC1(1286-1594) or TAX1BP1(1-312)/RB1CC1(1286-1594) complex to form a stable ternary complex (Fig. 4 A-C and *SI Appendix*, Fig. S18 E and F). Therefore, the NAP1 coiled-coil domain alone can directly compete with RB1CC1 coiled-coil for binding to the SKICH domain of TAX1BP1. In contrast, the NAP1(1-75) fragment, which includes a unique N-terminal Claw-binding FIR motif in addition to the SKICH-binding coiled-coil region (51), can readily interact with the binary TAX1BP1(1-237)/RB1CC1(1286-1594) complex to form a stable ternary complex with 2:2:2 stoichiometry (Fig. 4 D-F). Importantly, our previous study demonstrated that the FIR-defective NAP1(1-75) I9Q mutant lacks the ability to interact with the RB1CC1 Claw domain (51). In our SEC and analytical ultracentrifugation-based assays, this NAP1(1-75) I9Q mutant exhibits similar effects as NAP1(33-75) but not NAP1(1-75) (Fig. 4), suggesting that the NAP1(1-75) I9Q mutant is incapable of interacting with the binary TAX1BP1(1-237)/RB1CC1(1286-1594) complex to form a stable trimeric complex. Notably, our SEC-based assays showed that the R1375A mutation in RB1CC1(1286-1594), which can specifically disrupt the RB1CC1 coiled-coil/TAX1BP1 SKICH interaction, does not impede the formation of the TAX1BP1(1-237)/NAP1(1-75)/RB1CC1(1286-1594) ternary complex (*SI Appendix*, Fig. S19 A and B). Therefore, the formation of the stable TAX1BP1/NAP1/RB1CC1 ternary complex is not dependent on the interaction between the TAX1BP1 SKICH domain and RB1CC1 coiled-coil. However, the A114Q mutation of TAX1BP1(1-237), which can specifically disrupt the binding between TAX1BP1 SKICH and NAP1 coiled-coil (36), can dramatically decrease the formation of the stable TAX1BP1/NAP1/RB1CC1 ternary complex (*SI Appendix*, Fig. S19 C and D). Based on these biochemical results, we concluded that the NAP1 FIR/RB1CC1 Claw interaction and the NAP1

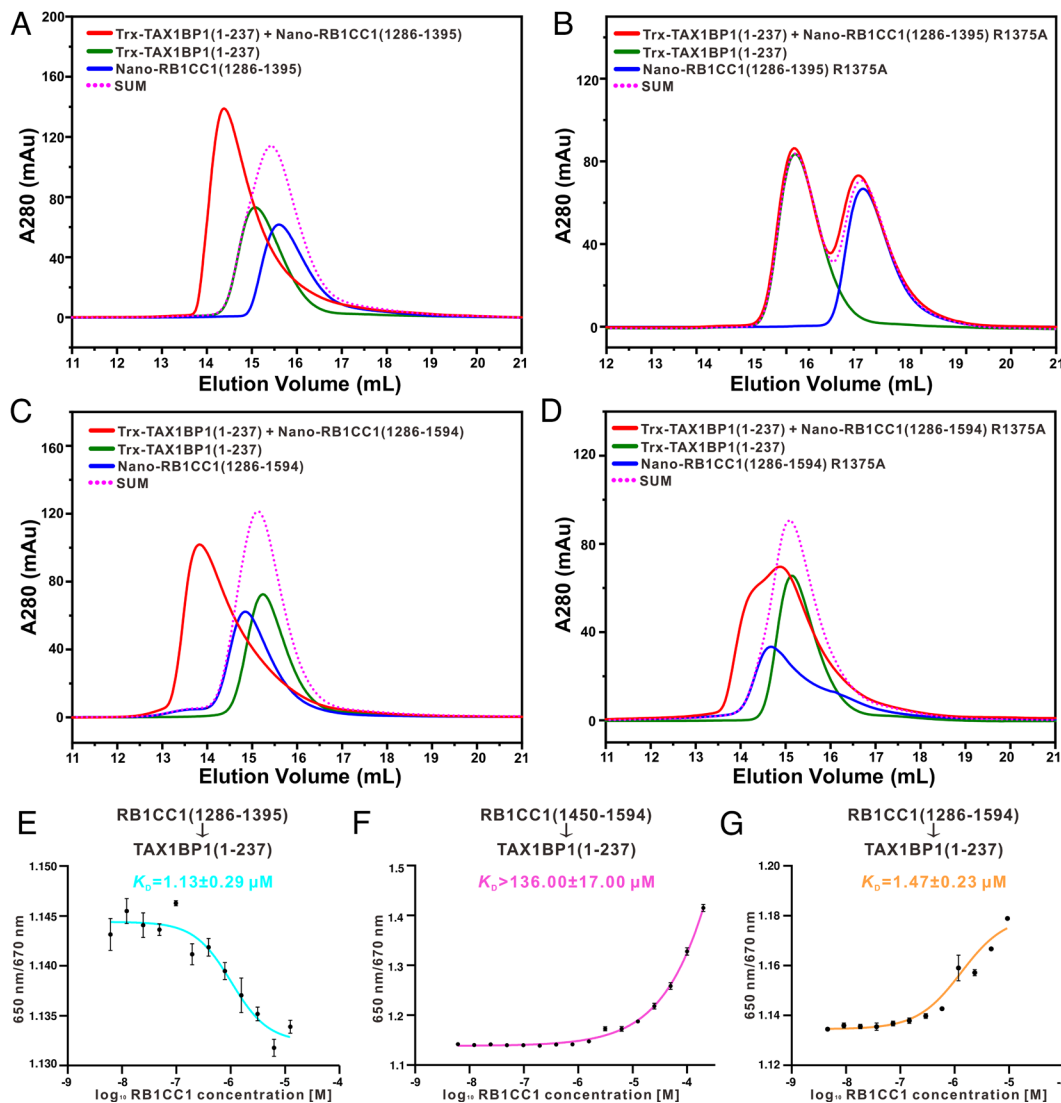


Fig. 3. There are two different binding sites between TAX1BP1 and RB1CC1. (A–D) SEC-based analyses of the interactions of RB1CC1(1286-1395) with TAX1BP1(1-237) (A), the RB1CC1(1286-1395) R1375A mutant with TAX1BP1(1-237) (B), RB1CC1(1286-1594) with TAX1BP1(1-237) (C), the RB1CC1(1286-1594) R1375A mutant with TAX1BP1(1-237) (D). (E–G) The measurement of the binding affinity of TAX1BP1(1-237) with RB1CC1(1286-1395) (E), RB1CC1(1450-1594) (F), or RB1CC1(1286-1594) (G), by the spectral shift binding assay. The spectral shift binding assays are conducted using 100 nM labeled TAX1BP1(1-237) titrated with different concentrations of RB1CC1(1286-1395), RB1CC1(1450-1594), or RB1CC1(1286-1594) in standard treated capillaries. The spectral shift fluorescence response caused by the ligand-binding at dual wavelengths (650 nm and 670 nm) is monitored by the Monolith X machine. The fitted curves and K_D values were determined using the Monolith Affinity Analysis K_D fit. Symbols and error bars represent the average data of three independent experiments and their SDs. Except for the spectral shift binding assays, the experiments depicted in this figure have been replicated once.

coiled-coil/TAX1BP1 SKICH interaction are essential for the formation of the stable TAX1BP1/NAP1/RB1CC1 ternary complex.

The CLIR Motif of TAX1BP1 Can Selectively Bind to Six Mammalian ATG8 Orthologs. Previously, a non-CLIR motif, specifically a Leu-Val-Val sequence, was identified in the loop region connecting the SKICH and coiled-coil domains of TAX1BP1 (30). It is worth noting that a similar CLIR motif was previously reported in NDP52, which selectively interacts with LC3C to facilitate the selective autophagy of invading bacteria mediated by NDP52 (47). To examine whether the CLIR motif of TAX1BP1 could discriminately bind to mammalian ATG8 proteins, we purified the TAX1BP1(123-151) fragment that contains the CLIR motif of TAX1BP1 and assessed its interactions with the six mammalian ATG8 orthologs. Using SEC-based analyses, we proved that TAX1BP1(123-151) can directly interact with mammalian ATG8 orthologs except for LC3A (Fig. 5A and SI Appendix, Fig. S20). Further ITC-based quantitative analyses of the interactions between TAX1BP1(123-151) and six mammalian ATG8 members revealed that TAX1BP1(123-151) exhibits a preference for binding to GABARAP and GABARAPL1 over other mammalian ATG8 family members. (Fig. 5B and C and SI Appendix, Fig. S21). Particularly, TAX1BP1(123-151) preferentially binds to GABARAP and GABARAPL1 with relatively small K_D values, 4.07 μM and 9.54 μM , respectively (Fig. 5B and C and SI Appendix, Fig. S21D). Consistent with our SEC result

(SI Appendix, Fig. S20A), TAX1BP1(123-151) is unable to recognize LC3A in our ITC-based assay (Fig. 5B and SI Appendix, Fig. S21A). Strikingly, further truncation and ITC-based analyses showed that the TAX1BP1(133-151) fragment, which includes the core CLIR region of TAX1BP1, displays a much weaker binding affinity toward GABARAP than the TAX1BP1(123-151) fragment (Fig. 5C and SI Appendix, Fig. S22A), while the N-terminal TAX1BP1(123-132) fragment is barely unable to interact with GABARAP in our ITC assay (Fig. 5C and SI Appendix, Fig. S22B), suggesting that the N-terminal region of TAX1BP1(123-151) can cooperate with the core Leu-Val-Val motif of TAX1BP1 to facilitate the interaction between TAX1BP1 and GABARAP. Notably, the N-terminal sequences preceding the core Leu-Val-Val motif of TAX1BP1 and NDP52 are quite different (Fig. 5D). Collectively, these findings demonstrated that TAX1BP1 possesses a unique CLIR motif, which is different from NDP52 and exhibits selective binding capabilities toward different mammalian ATG8 orthologs.

Overall Structure of the TAX1BP1 CLIR in Complex with GABARAP. By using the TAX1BP1(123-151)-GSGS-GABARAP fusion protein, wherein TAX1BP1(123-151) is directly fused to the N-terminal of GABARAP via a flexible GSGS linker, we successfully obtained high-quality crystals and subsequently determined the crystal structure of the TAX1BP1 CLIR/GABARAP complex to 1.53 Å resolution (SI Appendix, Table S1).

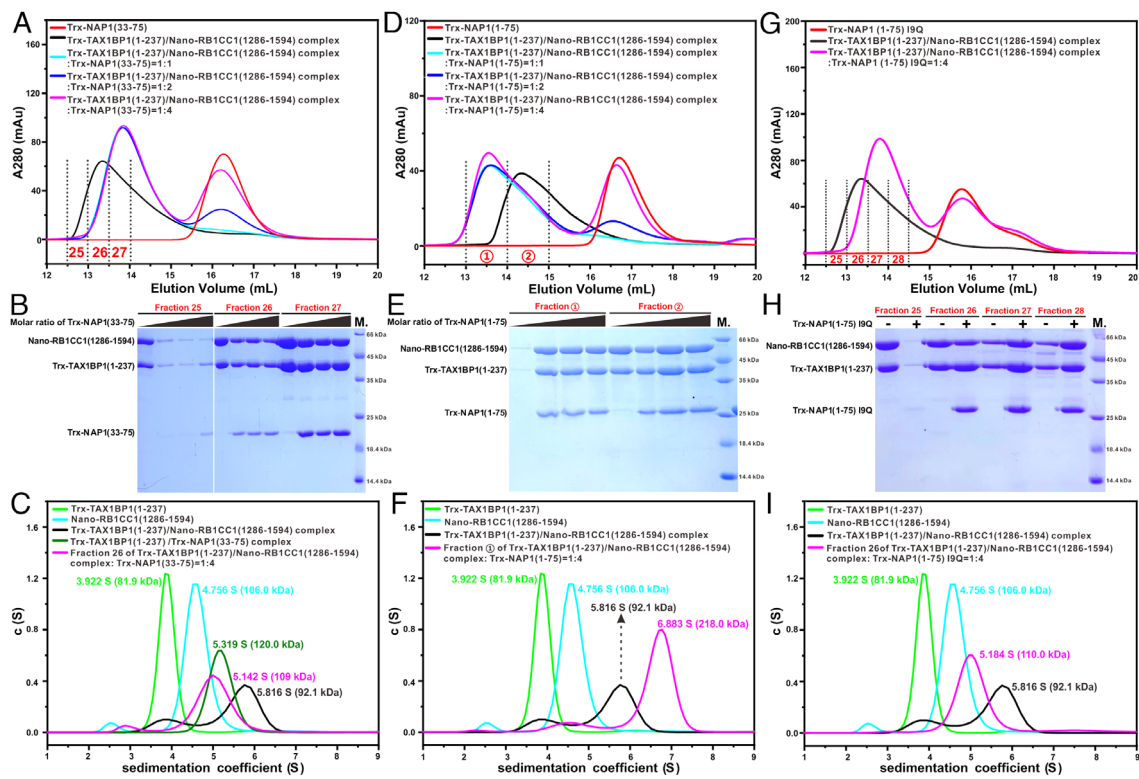


Fig. 4. The FIR motif of NAP1 is essential for the stable TAX1BP1/NAP1/RB1CC1 ternary complex formation. (A) SEC-based analyses of the TAX1BP1(1-237)/RB1CC1(1286-1594) complex incubated with increasing molar ratios of NAP1(33-75). (B) SDS-PAGE combined with Coomassie blue staining analyses showing the protein components of corresponding fractions collected from the SEC experiments of the TAX1BP1(1-237)/RB1CC1(1286-1594) complex incubated with increasing molar ratios of NAP1(33-75) in panel A. (C) Overlay plot of the sedimentation velocity data of TAX1BP1(1-237) (green), RB1CC1(1286-1594) (cyan), the TAX1BP1(1-237)/RB1CC1(1286-1594) complex (black), the TAX1BP1(1-237)/NAP1(33-75) complex (forest), and the fraction 26 collected from the SEC experiment of the TAX1BP1(1-237)/RB1CC1(1286-1594) complex incubated with 1:4 molar ratio of NAP1(33-75) in panel A. (D) SEC-based analyses of the TAX1BP1(1-237)/RB1CC1(1286-1594) complex incubated with increasing molar ratios of NAP1(1-75). (E) SDS-PAGE combined with Coomassie blue staining analyses showing the protein components of corresponding fractions collected from the SEC experiments of the TAX1BP1(1-237)/RB1CC1(1286-1594) complex incubated with increasing molar ratios of NAP1(1-75) in panel D. (F) Overlay plot of the sedimentation velocity data of TAX1BP1(1-237) (green), RB1CC1(1286-1594) (cyan), the TAX1BP1(1-237)/RB1CC1(1286-1594) complex (black), and the fraction ③ collected from the SEC experiment of the TAX1BP1(1-237)/RB1CC1(1286-1594) complex incubated with 1:4 molar ratio of NAP1(1-75) in panel D. (G) SEC-based analyses of the TAX1BP1(1-237)/RB1CC1(1286-1594) complex incubated with increasing molar ratios of the NAP1(1-75) I9Q mutant. (H) SDS-PAGE combined with Coomassie blue staining analyses showing the protein components of corresponding fractions collected from the SEC experiments of the TAX1BP1(1-237)/RB1CC1(1286-1594) complex incubated with increasing molar ratios of the NAP1(1-75) I9Q mutant in panel G. (I) Overlay plot of the sedimentation velocity data of TAX1BP1(1-237) (green), RB1CC1(1286-1594) (cyan), the TAX1BP1(1-237)/RB1CC1(1286-1594) complex (black), and the fraction 26 collected from the SEC experiment of the TAX1BP1(1-237)/RB1CC1(1286-1594) complex incubated with 1:4 molar ratio of the NAP1(1-75) I9Q mutant in panel G. Theoretical MW: Trx-TAX1BP1(1-237), 41.9 kDa; Nano-RB1CC1(1286-1594), 57.0 kDa; Trx-NAP1(33-75), 19.4 kDa; Trx-NAP1(1-75), 23.0 kDa. The experiments depicted in this figure have been replicated once.

In the final refined structural model, each asymmetric unit contains four 1:1 stoichiometric TAX1BP1 CLIR/GABARAP complexes (*SI Appendix*, Fig. S23A and Fig. 5E). In the TAX1BP1 CLIR/GABARAP complex structure, the GABARAP molecule adopts a typical ATG8 homolog protein folding, which is assembled by a four-stranded β -sheet together with four α -helices (Fig. 5E), and its overall conformation closely resembles the *apo*-form GABARAP structure (PDB ID: 1KJT) (*SI Appendix*, Fig. S23B). In the complex structure, the GABARAP-bound TAX1BP1 CLIR motif forms a unique architecture, mainly consisting of a two-stranded antiparallel β -sheet and a C-terminal short α -helix, and directly packs against the CLIR-binding groove of GABARAP formed by the α 1-, α 2-, and α 3-helices together with the β 2-strand of GABARAP, burying a total surface area of \sim 695 Å² (Fig. 5E and F). Notably, both N-terminal and C-terminal extensions of the core Leu-Val-Val motif of TAX1BP1 CLIR are directly involved in the interaction with GABARAP (Fig. 5E and F), which is distinct from the binding mode between NDP52 CLIR and LC3C (47).

The Molecular Interface of the TAX1BP1 CLIR/GABARAP Complex. Detailed structural analysis of the TAX1BP1 CLIR/GABARAP binding interface revealed that the specific interaction between TAX1BP1 CLIR and GABARAP is primarily mediated by

hydrophobic and polar interactions (Fig. 5F and G). Strikingly, unlike the typical LIR motif that contains a key aromatic residue to deeply embed in the hydrophobic pocket 1 (HP1) of an ATG8 family protein (52), the hydrophobic side chain of M140 residue of TAX1BP1 CLIR specifically situates at the HP1 of GABARAP assembled by the hydrophobic side chains of I21, P30, L50, and F104 as well as the aliphatic side chain of K48 residue (Fig. 5F and G and *SI Appendix*, Fig. S24B). Meanwhile, the hydrophobic side chain of V143 from TAX1BP1 CLIR occupies the corresponding hydrophobic pocket 2 (HP2) of GABARAP, which is formed by the Y49, V51, P52, L55, F60, F62, and L63 residues of GABARAP (Fig. 5F and G and *SI Appendix*, Fig. S24B). Furthermore, the hydrophobic side chains of L141, V142, and L150 residues together with the hydrophobic side group of T131 from TAX1BP1 CLIR form a continuous hydrophobic patch to pack against the hydrophobic groove of GABARAP formed by the typical HP2 as well as certain hydrophobic residues from HP1 (Fig. 5F and G). In addition, the backbone oxygen groups of S138, V143, G148, and L150 together with the side chain hydroxyl group of T131 from TAX1BP1 CLIR forms five hydrogen bonds with the side chains of K48, R28, Q59, and R67 residues from GABARAP (Fig. 5G). Moreover, the backbone groups of TAX1BP1 L141 and V143 residues form three strong backbone hydrogen bonds with the K48

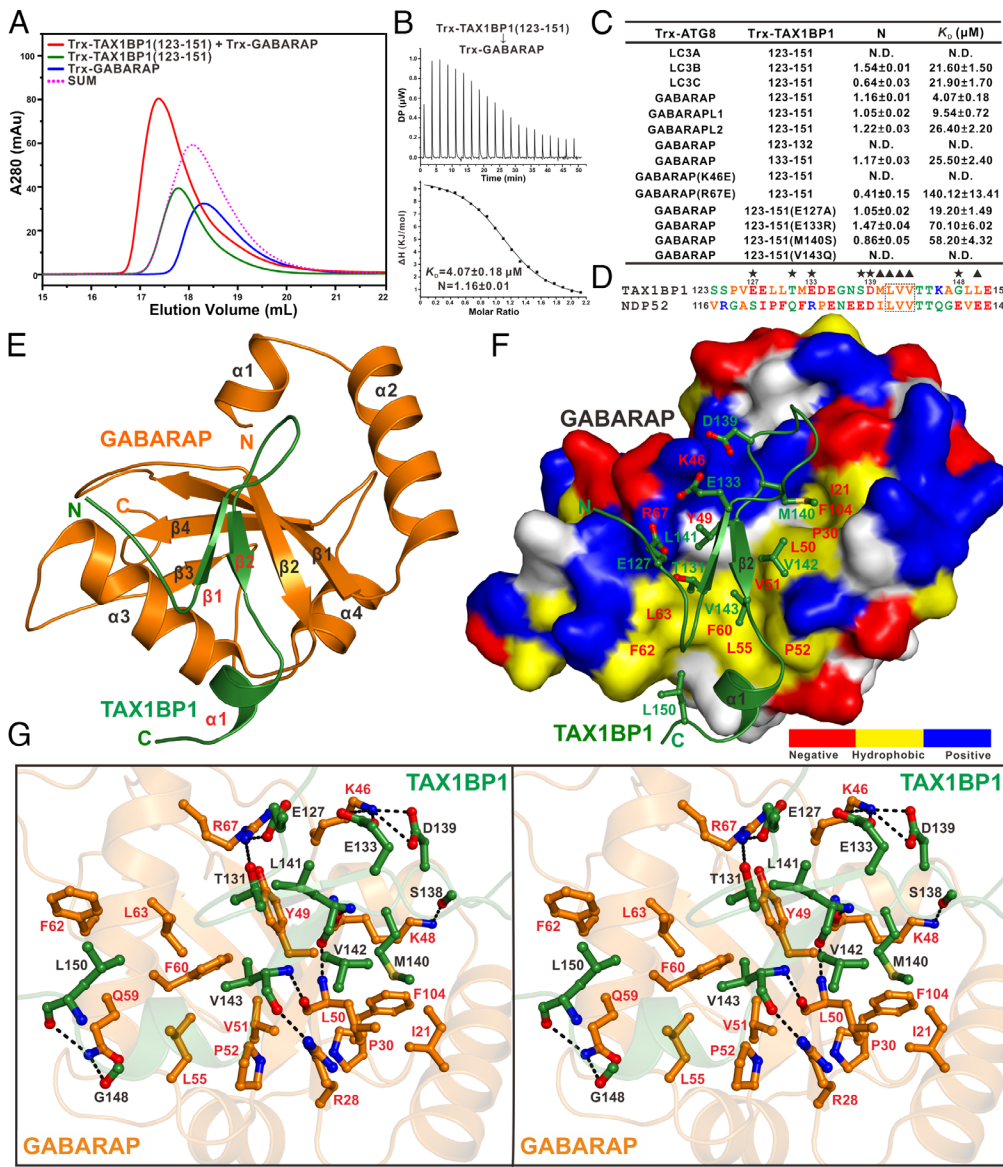


Fig. 5. Biochemical and structural analyses of the interactions of TAX1BP1 CLIR with mammalian ATG8 orthologs. (A) SEC-based analysis of the interaction between TAX1BP1(123-151) and GABARAP. (B) ITC-based measurement of the binding affinity of TAX1BP1(123-151) with GABARAP. The dissociation constant (K_D) error is the fitted error obtained from the data analysis software when using the one-site binding model to fit the ITC data. (C) The measured binding affinities between TAX1BP1 CLIR and six mammalian ATG8 family proteins or their mutants by ITC-based assays. “N.D.” stands for that the K_D value is not detectable. (D) Sequence alignment analysis of the CLIR regions of TAX1BP1 and NDP52. In this alignment, the interface residues of TAX1BP1 CLIR involved in the interactions with GABARAP are highlighted with black stars (polar interactions) or triangles (hydrophobic interactions). (E) Ribbon diagram showing the overall structure of the TAX1BP1 CLIR/GABARAP complex. In this drawing, GABARAP is colored in marine, while the bound TAX1BP1 CLIR molecule is colored in magentas. (F) The combined surface representation and ribbon-stick model showing the hydrophobic binding surface between TAX1BP1 CLIR and GABARAP. In this representation, GABARAP is shown in the surface model colored by different amino acid types, and TAX1BP1 CLIR is displayed in the ribbon-stick model. Specifically, the hydrophobic amino acid residues of GABARAP in the surface model are drawn in yellow, the positively charged residues in blue, the negatively charged residues in red, and the uncharged polar residues in gray. (G) Stereoview of the ribbon-stick representation showing the detailed interactions between GABARAP and TAX1BP1 CLIR. In this drawing, the side chains are shown as stick-ball mode, and the hydrogen bonds involved in the binding are shown as dotted lines. The experiments depicted in

of the key residues are shown in stick-ball mode, and the hydrogen bonds involved in the binding are shown as dotted lines. The experiments depicted in this figure have been replicated once.

and L50 residues located in the β 2-strand of GABARAP (Fig. 5 E and G). Strikingly, three specific charge–charge interactions found between the negatively charged E127, E133, and D139 residues of TAX1BP1 CLIR and the positively charged R67 and K46 residues of GABARAP further stabilize the TAX1BP1 CLIR/GABARAP complex formation. In agreement with their critical structural roles, all these key binding interface residues of TAX1BP1 CLIR are strictly conserved during evolution (SI Appendix, Fig. S2). Importantly, further comparison analyses of the TAX1BP1 CLIR/GABARAP complex with other currently known LIR/ATG8 family protein complexes, including the NDP52 CLIR/LC3C complex (PDB ID: 3VVW), the Optineurin LIR/LC3C complex (PDB ID: 2LUE), the p62 LIR/LC3C complex (PDB ID: 2ZJD), and the FAM134B LIR/LC3C complex (PDB ID: 7BRQ), revealed an unusual binding mode of LIR to ATG8 family proteins (SI Appendix, Fig. S24 A–F). Apparently, the characteristic binding mode of TAX1BP1 CLIR to GABARAP is endowed by the unique conformation of the two-stranded antiparallel β -sheet within TAX1BP1 CLIR, which enables the direct involvement of the N-terminal acidic E127, E133, D139 residues and the T131

residue of TAX1BP1 CLIR in the interaction with GABARAP (SI Appendix, Fig. S24B and Fig. 5 F and G). Notably, this type of LIR motif involving an intramolecular two-stranded antiparallel β -sheet was also identified in the pathogenic protein RavZ (53), TP53INP2 (54), FNIP (55), and the autophagy-related protein ATG3 (56) (SI Appendix, Fig. S24 G–I).

To further validate the interaction between TAX1BP1 CLIR and GABARAP observed in the TAX1BP1 CLIR/GABARAP complex structure, we conducted mutagenesis- and ITC-based analyses. In line with our structural data, individual point mutation of key binding interface residues either from TAX1BP1 or GABARAP, such as the E127A, E133R, M140S, and V143Q mutations of TAX1BP1(123-151) or the K46E and R67E mutations of GABARAP, significantly diminishes or completely disrupts the interaction between TAX1BP1(123-151) and GABARAP (SI Appendix, Fig. S25). Using relevant sequence alignment, biochemical and structural analyses, we also provided a mechanistic rationale for the selective binding of TAX1BP1 CLIR to different mammalian ATG8 orthologs (see SI Appendix, Results for a detailed description).

The Relationship between RB1CC1 and GABARAP in Binding to TAX1BP1. Given that TAX1BP1 interacts with RB1CC1 through its SKICH and coiled-coil domains, we inferred that the CLIR motif of TAX1BP1, which is located in the loop region between the SKICH and coiled-coil domains, might be accessible for engaging with ATG8 family proteins. Interestingly, our SEC coupled with sodium dodecyl sulfate-polyacrylamide gel electrophoresis (SDS-PAGE) assays showed that TAX1BP1(1-237) alone and the TAX1BP1(1-237)/RB1CC1(1286-1395) complex can readily interact with GABARAP (*SI Appendix*, Fig. S27 A–D), suggesting that the binding between TAX1BP1 SKICH and RB1CC1(1286-1395) region does not affect the TAX1BP1/GABARAP interaction. However, the inclusion of excess amount of GABARAP into the TAX1BP1(1-237)/RB1CC1(1286-1594) or TAX1BP1(1-312)/RB1CC1(1286-1594) binary complex results in a backward rather than a forward shift of the complex peak on the SEC profile (Fig. 6A and *SI Appendix*, Fig. S27E), suggesting RB1CC1(1286-1594), GABARAP and TAX1BP1 are unable to assemble a stable ternary complex. This notion is further supported by relevant SDS-PAGE and sedimentation velocity-based analyses (Fig. 6 B and C and *SI Appendix*, Fig. S27F). Notably, in addition to the SKICH-binding RB1CC1(1286-1395) region, RB1CC1(1286-1594) also includes the C-terminal coiled-coil and Claw region (residues 1450 to 1594) that can directly bind to the coiled-coil domain following the CLIR motif of TAX1BP1 (Fig. 3). Therefore, the interaction between RB1CC1(1450-1594) and the coiled-coil region of TAX1BP1 is likely to impede the TAX1BP1 CLIR/GABARAP interaction, due to potential steric exclusions. Indeed, based on the TAX1BP1 CLIR/GABARAP complex structure and the predicted structure model of the TAX1BP1(146-237)/RB1CC1(1450-1594) complex, the TAX1BP1(146-151) region not only can directly bind to GABARAP (Fig. 5 E–G) but also might be directly involved in the interaction with RB1CC1(1450-1594) (*SI Appendix*, Fig. S17A). Thus, without any additional proteins, the RB1CC1(1450-1594) region and ATG8 family protein are competitive in binding to TAX1BP1. It is worth noting that although GABARAP can compete with RB1CC1(1450-1594) for binding to TAX1BP1, it does not interfere the TAX1BP1 SKICH/RB1CC1 coiled-coil interaction. Therefore, RB1CC1(1286-1594) is unlikely to dissociate from the TAX1BP1(1-237)/GABARAP complex, and the competition between GABARAP and RB1CC1(1450-1594) for binding to TAX1BP1(1-237) is always existed. Accordingly, the binding ability of TAX1BP1(1-237) for GABARAP seems to be much stronger than that of TAX1BP1(1-237) in the presence of RB1CC1(1286-1594) (*SI Appendix*, Fig. S27 A and B and Fig. 6 A and B).

Strikingly, the inclusion of GABARAP into the ternary TAX1BP1(1-237)/NAP1(1-75)/RB1CC1(1286-1594) complex at 5:1 molar ratio leads to a forward shift of the complex peak on the SEC profile (Fig. 6D). Meanwhile, the addition of GABARAP into the ternary TAX1BP1(1-237)/NAP1(1-75)/RB1CC1(1286-1594) complex shows a larger sedimentation coefficient value than that of the ternary complex alone (Fig. 6F), indicating that GABARAP can further interact with the ternary TAX1BP1(1-237)/NAP1(1-75)/RB1CC1(1286-1594) complex to form a much larger GABARAP/TAX1BP1(1-237)/NAP1(1-75)/RB1CC1(1286-1594) quaternary complex. However, comparing with the isolated TAX1BP1(1-237), the TAX1BP1(1-237) in the ternary TAX1BP1(1-237)/NAP1(1-75)/RB1CC1(1286-1594) complex exhibits a significantly diminished capacity to recruit GABARAP (Fig. 6 D and E and *SI Appendix*, Fig. S27 A and B). Nevertheless, based on our biochemical results, when NAP1 is binding to the TAX1BP1/RB1CC1 complex, it has the ability to rearrange the association between TAX1BP1 and RB1CC1, thereby facilitating the recruitment of GABARAP by TAX1BP1. Furthermore, using

relevant biochemical and structural analyses, we elucidated that the recruitment of GABARAP into the TAX1BP1/RB1CC1/NAP1 complex relies on the CLIR motif of TAX1BP1 but not the FIR motif of NAP1 (see *SI Appendix*, *Results* for a detailed description).

Discussion

Previous functional studies have well demonstrated the vital roles of TAX1BP1 in relevant autophagy processes through its interaction with RB1CC1 (33, 34, 44, 45). In particular, TAX1BP1 is critical for the effective recruitment of RB1CC1 to p62/NBR1/TAX1BP1/poly-ubiquitin condensates to mediate the autophagic degradation of p62/poly-ubiquitin condensates in aggrephagy (33). Furthermore, the lysophagy process mediated by TAX1BP1 relies on its SKICH domain for associating with RB1CC1 (34). However, the detailed mechanism underlying the interaction between TAX1BP1 and RB1CC1 remains elusive. In this study, we have provided mechanistic insights into the interaction between TAX1BP1 and RB1CC1. Our findings demonstrate that in addition to the previously reported TAX1BP1 SKICH/RB1CC1 coiled-coil interaction, the first coiled-coil domain of TAX1BP1 can directly bind to the C-terminal coiled-coil and Claw region (residues 1450 to 1594) of RB1CC1 (Fig. 3). Thus, there are two distinct binding sites between TAX1BP1 and RB1CC1. Based on the quantitative K_D values measured by the spectral shift binding assays, the two binding sites of RB1CC1 (RB1CC1 coiled-coil and RB1CC1(1450-1594)) do not have a synergistic effect in binding to TAX1BP1 (Fig. 3 E–G). Thus, the two different binding sites between RB1CC1 and TAX1BP1 should endow RB1CC1 and TAX1BP1 to form dynamic oligomers. Indeed, based on our analytical ultracentrifugation-based result, the purified TAX1BP1(1-237)/RB1CC1(1286-1594) binary complex has a broad sedimentation coefficient distribution (Fig. 4C), suggesting the formation of an inhomogeneous TAX1BP1(1-237)/RB1CC1(1286-1594) binary complex with different oligomeric states. Accordingly, we failed to solve the structure of the TAX1BP1(1-237)/RB1CC1(1286-1594) complex either using X-ray crystallography or cryo-electron microscopy (Cryo-EM) method. The present study successfully determined the crystal structure of the TAX1BP1 SKICH domain in complex with the RB1CC1 coiled-coil, thereby elucidating the intricate binding mechanism and crucial factors responsible for the specific interaction between the TAX1BP1 SKICH domain and the RB1CC1 coiled-coil region (Fig. 2). Regrettably, due to unsuccessful crystallization, the precise mechanism underlying the identified TAX1BP1 coiled-coil/RB1CC1 (1450-1594) interaction remains unknown. However, based on our biochemical and structural modeling results (Fig. 3 and *SI Appendix*, Figs. S14 and S17A), the binding mode between TAX1BP1 coiled-coil and RB1CC1(1450-1594) should be different from that of the FIR/RB1CC1 Claw interaction. Nonetheless, more investigations are required to elucidate the detailed molecular mechanism underpinning the specific interaction between TAX1BP1 coiled-coil and RB1CC1(1450-1594) as well as the related potential function of this interaction in the context of TAX1BP1-mediated autophagy processes in the future.

Interestingly, through rigorous biochemical analyses, we have uncovered that the N-terminal coiled-coil domain (residues 33 to 75) of NAP1 has a good ability to compete with the coiled-coil domain of RB1CC1 for binding to the SKICH domain of TAX1BP1 (Fig. 4 A–C and *SI Appendix*, Fig. S18). Considering that the binding interface residues necessary for the interactions with RB1CC1 and NAP1 are located on the opposing surfaces of the TAX1BP1 SKICH domain (*SI Appendix*, Fig. S7C), there must be some allosteric effects on the SKICH domain of TAX1BP1 induced by the NAP1(33-75)-binding to impede the interaction

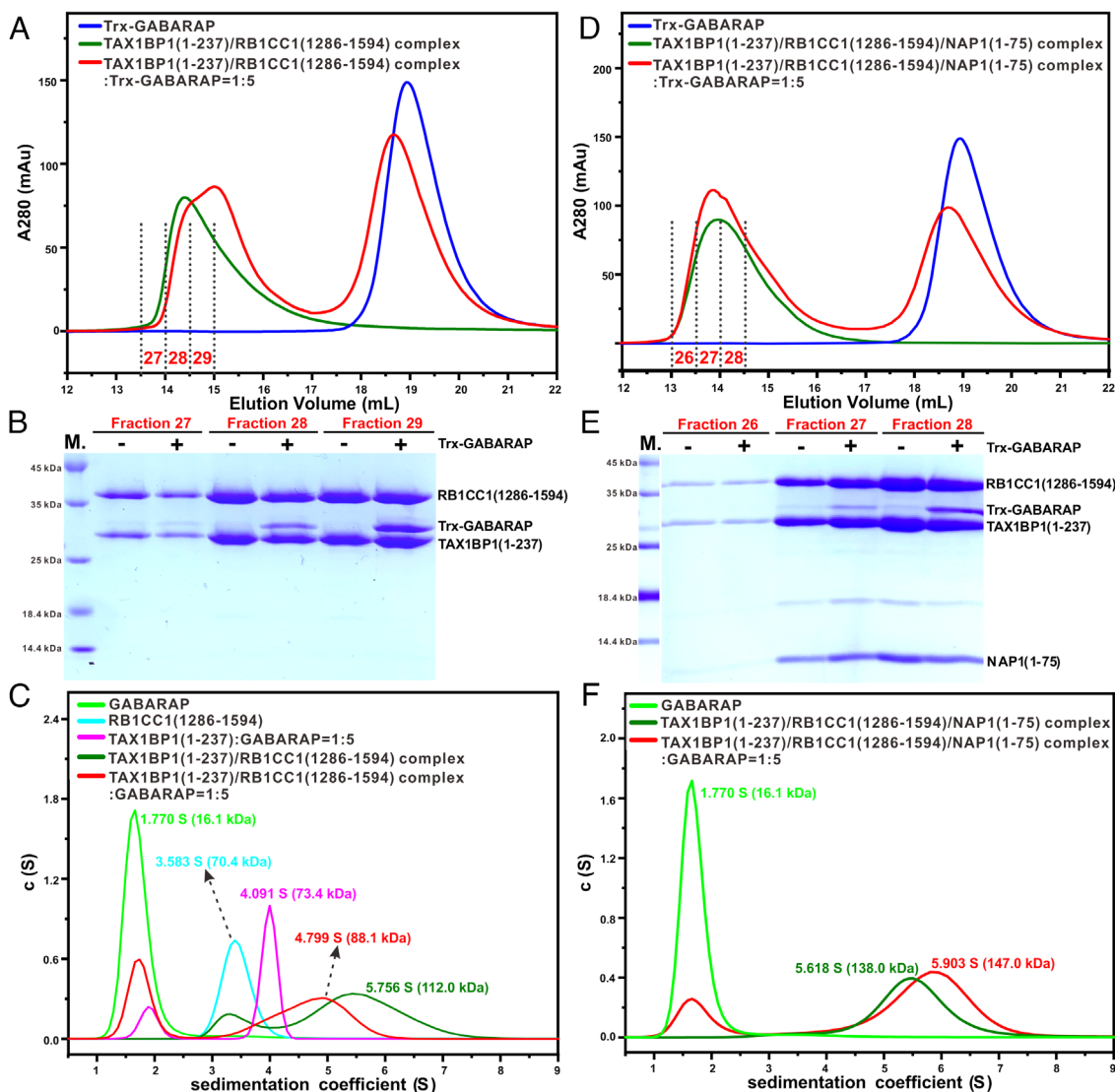


Fig. 6. The associations of NAP1 with RB1CC1 and TAX1BP1 facilitate the recruitment of GABARAP by TAX1BP1. (A) SEC-based analyses of the interactions of GABARAP with the TAX1BP1(1-237)/RB1CC1(1286-1594) binary complex. (B) SDS-PAGE combined with Coomassie blue staining analyses showing the protein components of corresponding fractions collected from the SEC experiments of GABARAP mixed with the TAX1BP1(1-237)/RB1CC1(1286-1594) in panel A. (C) Overlay plot of the sedimentation velocity data of GABARAP (green), RB1CC1(1286-1594) (cyan), the mixture of TAX1BP1(1-237) with GABARAP at 1:5 molar ratio (magenta), the TAX1BP1(1-237)/RB1CC1(1286-1594) complex (forest), and the mixture of the TAX1BP1(1-237)/RB1CC1(1286-1594) binary complex with GABARAP at 1:5 molar ratio (red). (D) SEC-based analyses of the interactions of GABARAP with the TAX1BP1(1-237)/NAP1(1-75)/RB1CC1(1286-1594) ternary complex. (E) SDS-PAGE combined with Coomassie blue staining analyses showing the protein components of corresponding fractions collected from the SEC experiments of GABARAP mixed with the TAX1BP1(1-237)/NAP1(1-75)/RB1CC1(1286-1594) ternary complex in panel D. (F) Overlay plot of the sedimentation velocity data of GABARAP (green), the TAX1BP1(1-237)/RB1CC1(1286-1594)/NAP1(1-75) ternary complex (forest), and the mixture of the TAX1BP1(1-237)/RB1CC1(1286-1594)/NAP1(1-75) ternary complex with GABARAP at 1:5 molar ratio (red). Theoretical MW: TAX1BP1(1-237), 27.6 kDa; RB1CC1(1286-1594), 35.4 kDa; NAP1(1-75), 8.6 kDa; GABARAP, 13.9 kDa. The experiments depicted in this figure have been replicated once.

between TAX1BP1 SKICH and RB1CC1 coiled-coil. Indeed, when comparing the crucial residues of TAX1BP1 SKICH in the RB1CC1-bound state and the NAP1-bound state, a comprehensive analysis showed that there are obviously conformational changes of several key residues of TAX1BP1 SKICH, such as the Y90 and Y91 residues (*SI Appendix*, Fig. S30A), and importantly, the configuration of TAX1BP1 Y91 residue in the NAP1-bound state is impossible to interact with RB1CC1 due to the potential steric hindrance (*SI Appendix*, Fig. S30B). Notably, a similar phenomenon is observed, when NAP1(33-75) engages with the SKICH domain of NDP52 that is associated with the coiled-coil domain of RB1CC1 (51). Based on the quantitative ITC results obtained in this study and a previous study from our group (36), the binding affinity between TAX1BP1 SKICH and NAP1 coiled-coil is stronger than that of the TAX1BP1 SKICH/RB1CC1 coiled-coil

interaction ($K_D \sim 2.05 \mu\text{M}$ versus $K_D \sim 4.91 \mu\text{M}$). Thus, the coiled-coil domain of NAP1 can easily compete with RB1CC1 for binding to the SKICH domain of TAX1BP1, thereby reducing the association between RB1CC1 and TAX1BP1 (*SI Appendix*, Fig. S18). Based on these biochemical results, we inferred that TAX1BP1 should initially interact with RB1CC1 *in vivo* followed by binding to NAP1. Notably, the FIR motif of NAP1, which can specifically bind to the Claw domain of RB1CC1 based on our previous study (51), is essential for the formation of the stable TAX1BP1/NAP1/RB1CC1 ternary complex (Fig. 4). Therefore, we speculated that when NAP1 is binding to the TAX1BP1/RB1CC1 complex, NAP1 can directly rearrange the interaction between TAX1BP1 and RB1CC1. In particular, the NAP1 coiled-coil domain displaces the RB1CC1 coiled-coil domain from binding to the TAX1BP1 SKICH domain, and the NAP1 FIR

motif displaces the TAX1BP1 coiled-coil domain for binding to the RB1CC1(1450–1594) region, thereby resulting in the formation of the stable TAX1BP1/NAP1/RB1CC1 complex (Fig. 4 D–F). Although the precise mechanism for the assembly of the trimeric TAX1BP1/NAP1/RB1CC1 complex is still unknown, our findings suggested that the assembling mode of the trimeric TAX1BP1/NAP1/RB1CC1 complex involves the binding of NAP1 to RB1CC1 Claw through its FIR domain as well as the binding of NAP1 to TAX1BP1 SKICH through its coiled-coil domain. In the future, we hope to solve this trimeric TAX1BP1/NAP1/RB1CC1 complex structure to uncover its unique assembling mechanism using X-ray crystallography or Cryo-EM approach.

The associations between autophagy receptors and TBK1 as well as the activation of the kinase activity of TBK1 were well demonstrated to play critical roles in promoting different forms of selective autophagy mediated by p62, Optineurin, and NDP52 (17, 32, 37–40, 50, 57). Particularly, Optineurin can directly employ the TBK1 kinase to recruit the PI3KC3-C1 complex to initiate the PINK1/Parkin-dependent mitophagy process (40). NAP1 is a TBK1-binding adaptor protein (15, 36, 58), which can directly bind to TBK1 kinase through its C-terminal TBD domain (Fig. 1A). Therefore, the binding of NAP1 with TAX1BP1 not only can stabilize the trimeric TAX1BP1/NAP1/RB1CC1 complex, but also may directly recruit the TBK1 kinase to further facilitate the assembly of a quaternary TAX1BP1/NAP1/RB1CC1/TBK1 complex as well as the subsequent recruitment of the PI3KC3-C1 complex for initiating selective autophagy. Indeed, our biochemical assays demonstrated that the TAX1BP1(1–237)/RB1CC1(1286–1594) complex can directly interact with the NAP1(1–254)/TBK1 complex to form a stable quaternary complex (*SI Appendix*, Fig. S31). Importantly, a recent study showed that the A114Q mutation of TAX1BP1, which can specifically disrupt the interaction between TAX1BP1 SKICH and NAP1, severely blocked the TAX1BP1-dependent lysophagy process (34). Interestingly, TBK1 can directly phosphorylate TAX1BP1 on multiple sites (37). However, the relevant downstream effects of the TBK1-mediated phosphorylation of TAX1BP1 as well as the precise role of TBK1 during selective autophagy driven by TAX1BP1 remain unclear. Intriguingly, a recent report showed that TBK1 is not essential for the initiation of NDP52-mediated mitophagy but may regulate the efficiency of mitophagy initiation by NDP52 (40), which can adopt a similar way as TAX1BP1 to recruit TBK1 by binding to NAP1 (36). Therefore, in order to gain a comprehensive understanding of the significance of the TAX1BP1/NAP1/RB1CC1/TBK1 complex formation and the molecular mechanism by which TAX1BP1 initiates selective autophagy, a thorough examination of the roles of TBK1 and the ULK complex in different TAX1BP1-mediated selective autophagy processes is required in the future.

In this study, we have solved the crystal structure of the non-canonical CLIR motif of TAX1BP1 in complex with GABARAP, and elucidated the detailed molecular mechanism underlying the selective recognitions of mammalian ATG8 family proteins by TAX1BP1. Importantly, the determined TAX1BP1 CLIR/GABARAP complex structure reveals a unique binding mode adopted by the CLIR motif of TAX1BP1 to interact with GABARAP, which is distinct from the currently known NDP52 CLIR/LC3C binding mode (47), thereby enriching the repertoire of the CLIR/ATG8 family protein interaction modes. Notably, unlike p62 and NDP52, both of which rely on their LIR regions to interact with the Claw domain of RB1CC1 (51, 59), TAX1BP1 mainly employs the coiled-coil region following its CLIR motif to recognize the extreme C-terminal coiled-coil and Claw region of RB1CC1, confirming the notion that TAX1BP1 and NDP52 are two different and functionally nonredundant autophagy receptors.

Interestingly, based on our biochemical results, ATG8 family proteins, RB1CC1 and TAX1BP1 are unable to form a stable ternary complex, similar to that of p62 and NDP52 (51, 59). Therefore, the recruitments of ULK complex and ATG8 family proteins during TAX1BP1-mediated selective autophagy processes are likely to be asynchronous. In addition to its canonical role as an autophagy receptor to drive selective autophagy, TAX1BP1 can also promote amphisome formation by interacting with the actin-based motor Myosin VI and ATG8 family proteins decorated on the outer surface of autophagosome (16, 31, 48, 49). Meanwhile, TAX1BP1 can associate with RB1CC1 to mediate several non-canonical ATG8-independent autophagy processes (44, 45). Apparently, during these distinct autophagic processes, different ATG8-binding ability of TAX1BP1 might be required. Indeed, we noticed that TAX1BP1 alone, the binary TAX1BP1/RB1CC1 complex and the ternary TAX1BP1/NAP1/RB1CC1 complex have distinct abilities to interact with ATG8 family protein. Thus, our findings in this work may also provide a plausible mechanistic explanation for the multiple autophagic functions mediated by TAX1BP1.

To gain further mechanistic insights into the interaction of the TAX1BP1/RB1CC1/NAP1 ternary complex with ATG8 family protein, we also sought to predict the structure of the TAX1BP1/RB1CC1/NAP1/GABARAP complex using ColabFold. Regrettably, the predicted structure model of the TAX1BP1/RB1CC1/NAP1/GABARAP complex is not very reasonable. As an alternative, we tried the structure prediction of the TAX1BP1(1–237)/RB1CC1(1286–1594)/NAP1(1–75) ternary complex (*SI Appendix*, Fig. S32). Although the interaction between NAP1 FIR and RB1CC1 Claw in the predicted complex structure is not fully correct, the spatial arrangement of TAX1BP1(1–237), RB1CC1(1286–1594), and NAP1(1–75) within the complex model is in accord with our experimental data. Particularly, within the ternary complex, NAP1 binds to RB1CC1 via its FIR motif, and NAP1 binds to TAX1BP1 via its SKICH domain (*SI Appendix*, Fig. S32). Importantly, further comparison of the TAX1BP1 CLIR/GABARAP complex structure with the predicted TAX1BP1(1–237)/RB1CC1(1286–1594)/NAP1(1–75) complex structure revealed that the binding of GABARAP with TAX1BP1/NAP1/RB1CC1 ternary complex is spatially feasible, but the orientation does not allow for a perfect binding as observed in the TAX1BP1 CLIR/GABARAP complex structure (*SI Appendix*, Fig. S32), which may partially explain why the TAX1BP1/NAP1/RB1CC1 ternary complex exhibits a significantly diminished capacity to recruit GABARAP compared with TAX1BP1.

Finally, based on our findings in this study together with previous relevant reports, we proposed a model to depict the intricate relationship between TAX1BP1, the RB1CC1-containing ULK complex, the NAP1/TBK1 complex, and ATG8 family proteins during the initiation of selective autophagy process mediated by TAX1BP1 (*SI Appendix*, Fig. S33). In this model, relevant autophagic cargo, such as the ubiquitinated invading pathogen or dysfunctional lysosome, is initially recognized by TAX1BP1 through its C-terminal Ub-binding zinc finger domain (*SI Appendix*, Fig. S33). Then, TAX1BP1 recruits the ULK complex through a dual-binding site mode between the N-terminal SKICH and coiled-coil region of TAX1BP1 and the C-terminal coiled-coil and Claw region of RB1CC1 uncovered in this study (*SI Appendix*, Fig. S33). Notably, the interaction between TAX1BP1 and RB1CC1 not only can specifically hinder the CLIR motif of TAX1BP1 for binding to ATG8 family proteins, but also may lead to the oligomerization of the ULK complex and the subsequent activation of the ULK complex. Whereafter, the activated ULK complex could *in situ* initiate phagophore formation by recruiting relevant downstream autophagic machinery, such as the PI3KC3-C1 complex (*SI Appendix*, Fig. S33). In parallel, the NAP1/TBK1 complex could also be recruited by TAX1BP1 through the adaptor protein

NAP1 (*SI Appendix*, Fig. S33). This recruitment would rearrange the interaction between TAX1BP1 and RB1CC1 and induces the formation of the ULK/TAX1BP1/NAP1/TBK1 super-complex as well as the release of the CLIR in TAX1BP1 for further interacting with the ATG8 family proteins decorated on the nascent phagophore membrane (*SI Appendix*, Fig. S33), thereby facilitating the recruitment of additional downstream autophagic machinery and the ultimate formation of autophagosome around the autophagic cargo specifically recognized by TAX1BP1.

Materials and Methods

Proteins used in this study were expressed in BL21 (DE3) *Escherichia coli* cells or in HEK293F cells, and purified by affinity chromatography followed by size-exclusion chromatography or ion-exchange chromatography. Crystals were obtained by the sitting drop vapor diffusion method at 16 °C. An extended description of the materials and methods for plasmid constructions, protein expression and purification,

NMR spectroscopy, crystallography, and relevant biochemical and cellular assays is included in *SI Appendix, Materials and Methods*.

Coordinates. The atomic coordinates and structure factors of the crystal structures of the TAX1BP1(1–121)/RB1CC1(1286–1395) complex and the TAX1BP1 CLIR/GABARAP complex have been deposited in the Protein Data Bank under the accession code 8W6B and 8W6A, respectively.

Data, Materials, and Software Availability. All study data are included in the article and/or *SI Appendix*.

ACKNOWLEDGMENTS. We thank SSRF BL02U1, and BL19U1 for X-ray beam time, Prof. Jiahui Han for the full length RB1CC1 and TAX1BP1 cDNA, and Dr. Chengjiang Gao for the NAP1 plasmid. This work was supported by grants from the National Natural Science Foundation of China (32071219, 92253301, 21822705), the CAS Youth Interdisciplinary Team (JCTD-2022-10), the National Basic Research Program of China (2022YFC2303102), and the Science and Technology Commission of Shanghai Municipality (20XD1425200) (to L.P.).

1. D. J. Klionsky, S. D. Emr, Cell biology—Autophagy as a regulated pathway of cellular degradation. *Science* **290**, 1717–1721 (2000).
2. H. Yamamoto, S. D. Zhang, N. Mizushima, Autophagy genes in biology and disease. *Nat. Rev. Genet.* **24**, 382–400 (2023).
3. I. Dikic, Z. Elazar, Mechanism and medical implications of mammalian autophagy. *Nat. Rev. Mol. Cell Biol.* **19**, 349–364 (2018).
4. B. Levine, G. Kroemer, Biological functions of autophagy genes: A disease perspective. *Cell* **176**, 11–42 (2019).
5. H. Nakatogawa, K. Suzuki, Y. Kamada, Y. Ohsumi, Dynamics and diversity in autophagy mechanisms: Lessons from yeast. *Nat. Rev. Mol. Cell Bio.* **10**, 458–467 (2009).
6. A. Stoltz, A. Ernst, I. Dikic, Cargo recognition and trafficking in selective autophagy. *Nat. Cell Biol.* **16**, 495–501 (2014).
7. E. Adrienne, L. Ferrari, S. Martens, Orchestration of selective autophagy by cargo receptors. *Curr. Biol.* **32**, R1357–R1371 (2022).
8. J. N. S. Vargas, M. Hamasaki, T. Kawabata, R. J. Youle, T. Yoshimori, The mechanisms and roles of selective autophagy in mammals. *Nat. Rev. Mol. Cell Biol.* **24**, 167–185 (2023).
9. V. Rogov, V. Dotsch, T. Johansen, V. Kirk, Interactions between autophagy receptors and ubiquitin-like proteins form the molecular basis for selective autophagy. *Mol. Cell* **53**, 167–178 (2014).
10. V. Kirk, V. V. Rogov, A diversity of selective autophagy receptors determines the specificity of the autophagy pathway. *Mol. Cell* **76**, 268–285 (2019).
11. S. Pankiv *et al.*, p62/SQSTM1 binds directly to Atg8/LC3 to facilitate degradation of ubiquitinated protein aggregates by autophagy. *J. Biol. Chem.* **282**, 24131–24145 (2007).
12. V. Kirk *et al.*, A role for NBR1 in autophagosomal degradation of ubiquitinated substrates. *Mol. Cell* **33**, 505–516 (2009).
13. J. Korac *et al.*, Ubiquitin-independent function of optineurin in autophagic clearance of protein aggregates. *J. Cell Sci.* **126**, 580–592 (2013).
14. S. A. Sarraf *et al.*, Loss of TAX1BP1-directed autophagy results in protein aggregate accumulation in the brain. *Mol. Cell* **80**, 779–795.e10 (2020).
15. T. L. Thurston, G. Ryzhakov, S. Bloor, N. von Muhlinen, F. Rando, The TBK1 adaptor and autophagy receptor NDP52 restricts the proliferation of ubiquitin-coated bacteria. *Nat. Immunol.* **10**, 1215–1221 (2009).
16. D. A. Tumbarello *et al.*, The autophagy receptor TAX1BP1 and the molecular motor myosin VI are required for clearance of salmonella typhimurium by autophagy. *PLoS Pathog.* **11**, e1005174 (2015).
17. P. Wild *et al.*, Phosphorylation of the autophagy receptor optineurin restricts Salmonella growth. *Science* **333**, 228–233 (2011).
18. I. Novak *et al.*, Nix is a selective autophagy receptor for mitochondrial clearance. *EMBO Rep.* **11**, 45–51 (2010).
19. L. Liu *et al.*, Mitochondrial outer-membrane protein FUNDC1 mediates hypoxia-induced mitophagy in mammalian cells. *Nat. Cell Biol.* **14**, 177–185 (2012).
20. M. D. Smith *et al.*, CCPG1 is a non-canonical autophagy cargo receptor essential for ER-phagy and pancreatic ER proteostasis. *Dev. Cell* **44**, 217–232.e11 (2018).
21. A. Khaminets *et al.*, Regulation of endoplasmic reticulum turnover by selective autophagy. *Nature* **522**, 354–358 (2015).
22. F. Fumagalli *et al.*, Translocon component Sec62 acts in endoplasmic reticulum turnover during stress recovery. *Nat. Cell Biol.* **18**, 1173–1184 (2016).
23. P. Grumati *et al.*, Full length RTN3 regulates turnover of tubular endoplasmic reticulum via selective autophagy. *Elife* **6**, e25555 (2017).
24. H. An *et al.*, TEX264 is an endoplasmic reticulum-resident ATG8-interacting protein critical for ER remodeling during nutrient stress. *Mol. Cell* **74**, 891–908.e10 (2019).
25. H. Chino, T. Hatta, T. Natsume, N. Mizushima, Intrinsically disordered protein TEX264 mediates ER-phagy. *Mol. Cell* **74**, 909–921.e6 (2019).
26. Q. Z. Chen *et al.*, ATL3 is a tubular ER-phagy receptor for GABARAP-mediated selective autophagy. *Curr. Biol.* **29**, 846–855.e6 (2019).
27. S. X. Jiang, C. D. Wells, P. J. Roach, Starch-binding domain-containing protein 1 (Stbd1) and glycogen metabolism: Identification of the Atg8 family interacting motif (AIM) in Stbd1 required for interaction with GABARAP1. *Biochem. Biophys. Res. Commun.* **413**, 420–425 (2011).
28. J. D. Mancias, X. X. Wang, S. P. Gygi, J. W. Harper, A. C. Kimmelman, Quantitative proteomics identifies NCOA4 as the cargo receptor mediating ferritinophagy. *Nature* **509**, 105–109 (2014).
29. F. Gachon *et al.*, CREB-2, a cellular CRE-dependent transcription repressor, functions in association with Tax as an activator of the human T-cell leukemia virus type 1 promoter. *J. Virol.* **72**, 8332–8337 (1998).
30. A. C. Newman *et al.*, TBK1 kinase addiction in lung cancer cells is mediated via autophagy of Tax1bp1/Ndp52 and non-canonical NF-κappa B signalling. *PLoS One* **7**, e50672 (2012).
31. D. A. Tumbarello *et al.*, Autophagy receptors link myosin VI to autophagosomes to mediate Tom1-dependent autophagosome maturation and fusion with the lysosome. *Nat. Cell Biol.* **14**, 1024–1035 (2012).
32. M. Lazarou *et al.*, The ubiquitin kinase PINK1 recruits autophagy receptors to induce mitophagy. *Nature* **524**, 309–314 (2015).
33. E. Turco *et al.*, Reconstitution defines the roles of p62, NBR1 and TAX1BP1 in ubiquitin condensate formation and autophagy initiation. *Nat. Commun.* **12**, 5212 (2021).
34. V. V. Eapen, S. Swarup, M. J. Hoyer, J. A. Paulo, J. W. Harper, Quantitative proteomics reveals the selectivity of ubiquitin-binding autophagy receptors in the turnover of damaged lysosomes by lysophagy. *Elife* **10**, e72328 (2021).
35. L. Ling, D. V. Goeddel, T6BP, a TRAF6-interacting protein involved in IL-1 signaling. *Proc. Natl. Acad. Sci. U.S.A.* **97**, 9567–9572 (2000).
36. T. Fu *et al.*, Mechanistic insights into the interactions of NAP1 with the SK1CH domains of NDP52 and TAX1BP1. *Proc. Natl. Acad. Sci. U.S.A.* **115**, E11651–E11660 (2018).
37. B. Richter *et al.*, Phosphorylation of OPTN by TBK1 enhances its binding to Ub chains and promotes selective autophagy of damaged mitochondria. *Proc. Natl. Acad. Sci. U.S.A.* **113**, 4039–4044 (2016).
38. G. Matsumoto, T. Shimogori, N. Hattori, N. Nukina, TBK1 controls autophagosomal engulfment of polyubiquitinated mitochondria through p62/SQSTM1 phosphorylation. *Hum. Mol. Genet.* **24**, 4429–4442 (2015).
39. J. M. Heo, A. Ordureau, J. A. Paulo, J. Rinehart, J. W. Harper, The PINK1–PARKIN mitochondrial ubiquitylation pathway drives a program of OPTN/NDP52 recruitment and TBK1 activation to promote mitophagy. *Mol. Cell* **60**, 7–20 (2015).
40. T. N. Nguyen *et al.*, Unconventional initiation of PINK1/Parkin mitophagy by Optineurin. *Mol. Cell* **83**, 1693–1709.e9 (2023).
41. F. X. Li *et al.*, Structural insights into the interaction and disease mechanism of neurodegenerative disease-associated optineurin and TBK1 proteins. *Nat. Commun.* **7**, 12708 (2016).
42. J. H. Hurley, L. N. Young, Mechanisms of autophagy initiation. *Ann. Rev. Biochem.* **86**, 225–244 (2017).
43. B. J. Ravenhill *et al.*, The cargo receptor NDP52 initiates selective autophagy by recruiting the ULK complex to cytosol-invading bacteria. *Mol. Cell* **74**, 320–329.e6 (2019).
44. A. E. Ohnstad *et al.*, Receptor-mediated clustering of FIP200 bypasses the role of LC3 lipidation in autophagy. *EMBO J.* **39**, e104948 (2020).
45. J. M. Goodwin *et al.*, Autophagy-independent lysosomal targeting regulated by ULK1/2–FIP200 and ATG9. *Cell Rep.* **20**, 2341–2356 (2017).
46. Y. Yang, G. Wang, X. L. Huang, Z. H. Du, Crystallographic and modelling studies suggest that the SK1CH domains from different protein families share a common Ig-like fold but harbour substantial structural variations. *J. Biomol. Struct. Dyn.* **33**, 1385–1398 (2015).
47. N. von Muhlinen *et al.*, LC3C, bound selectively by a noncanonical LIR motif in NDP52, is required for antibacterial autophagy. *Mol. Cell* **48**, 329–342 (2012).
48. S. C. Hu *et al.*, Mechanistic insights into recognitions of ubiquitin and myosin VI by autophagy receptor TAX1BP1. *J. Mol. Biol.* **430**, 3283–3296 (2018).
49. S. C. Hu *et al.*, Structure of Myosin VI/Tom1 complex reveals a cargo recognition mode of Myosin VI for tethering. *Nat. Commun.* **10**, 3459 (2019).
50. J. N. S. Vargas *et al.*, Spatiotemporal control of ULK1 activation by NDP52 and TBK1 during selective autophagy. *Mol. Cell* **74**, 347–362.e6 (2019).
51. T. Fu *et al.*, Structural and biochemical advances on the recruitment of the autophagy-initiating ULK and TBK1 complexes by autophagy receptor NDP52. *Sci. Adv.* **7**, eabi6582 (2021).
52. T. Johansen, T. Lamark, Selective autophagy: ATG8 family proteins, LIR motifs and cargo receptors. *J. Mol. Biol.* **432**, 80–103 (2020).
53. D. H. Kwon *et al.*, A novel conformation of the LC3-interacting region motif revealed by the structure of a complex between LC3B and RavZ. *Biochem. Biophys. Res. Commun.* **490**, 1093–1099 (2017).
54. S. W. Park *et al.*, Development of new tools to study membrane-anchored mammalian Atg8 proteins. *Autophagy* **19**, 1424–1443 (2023).
55. J. M. Goodwin *et al.*, GABARAP sequesters the FLCN–FNIP tumor suppressor complex to couple autophagy with lysosomal biogenesis. *Sci. Adv.* **7**, eabi2485 (2021).
56. J. Famung *et al.*, Semisynthetic LC3 probes for autophagy pathways reveal a noncanonical LC3 interacting region motif crucial for the enzymatic activity of human ATG3. *ACS Cent. Sci.* **9**, 1025–1034 (2023).
57. A. S. Moore, E. L. Holzbaur, Dynamic recruitment and activation of ALS-associated TBK1 with its target optineurin are required for efficient mitophagy. *Proc. Natl. Acad. Sci. U.S.A.* **113**, E3349–E3358 (2016).
58. G. Ryzhakov, F. Rando, SINTBAD, a novel component of innate antiviral immunity, shares a TBK1-binding domain with NAP1 and TANK. *EMBO J.* **26**, 3180–3190 (2007).
59. E. Turco *et al.*, FIP200 claw domain binding to p62 promotes autophagosome formation at ubiquitin condensates. *Mol. Cell* **74**, 330–346.e11 (2019).